



HAL
open science

Assessment of relative dispersion in the Gulf of Tonkin using numerical modeling and HF radar observations of surface currents

Manh Cuong Tran, Alexei Sentchev, Stefano Berti, Nadia K Ayoub, Tung Nguyen-Duy, Nguyen Kim Cuong

► To cite this version:

Manh Cuong Tran, Alexei Sentchev, Stefano Berti, Nadia K Ayoub, Tung Nguyen-Duy, et al.. Assessment of relative dispersion in the Gulf of Tonkin using numerical modeling and HF radar observations of surface currents. *Continental Shelf Research*, 2022, 245, pp.104784. 10.1016/j.csr.2022.104784 . hal-03921349

HAL Id: hal-03921349

<https://hal.science/hal-03921349>

Submitted on 9 Feb 2023

HAL is a multi-disciplinary open access archive for the deposit and dissemination of scientific research documents, whether they are published or not. The documents may come from teaching and research institutions in France or abroad, or from public or private research centers.

L'archive ouverte pluridisciplinaire **HAL**, est destinée au dépôt et à la diffusion de documents scientifiques de niveau recherche, publiés ou non, émanant des établissements d'enseignement et de recherche français ou étrangers, des laboratoires publics ou privés.

1 **Assessment of relative dispersion in the Gulf of Tonkin using numerical modeling and** 2 **HF radar observations of surface currents**

3
4 Manh Cuong Tran ^{1, 2, 5}, Alexei Sentchev ^{1, 5}, Stefano Berti ³, Nadia K. Ayoub ^{4, 5}, Tung Nguyen-Duy ^{4, 5},
5 Nguyen Kim Cuong ⁶

6
7 (1) Laboratory of Oceanology and Geosciences, UMR 8187, CNRS, Univ. Littoral Côte d'Opale, Univ. Lille,
8 IRD, 62930 Wimereux, France

9 (2) Center for Oceanography (CFO), Vietnam Administration of Seas and Islands (VASI), 8 Phao Dai Lang,
10 Dong Da, Hanoi, Vietnam

11 (3) Univ. Lille, ULR 7512, Unité de Mécanique de Lille Joseph Boussinesq (UML), 59000 Lille, France

12 (4) LEGOS, UMR5566, IRD, CNES, CNRS, Université de Toulouse, 31400 Toulouse, France

13 (5) LOTUS Laboratory, University of Science and Technology of Hanoi, Vietnam Academy of Science and
14 Technology, Hanoi, Vietnam

15 (6) VNU University of Science, Vietnam National University, 334 Nguyen Trai, Thanh Xuan, Hanoi, Vietnam

16 17 ABSTRACT

18 Particle pair statistics from synthetic drifter trajectories reconstructed from realistic, high-resolution numerical
19 simulations (SYMPHONIE model) and HF radar velocity measurements are used to investigate the dispersion
20 properties in the Gulf of Tonkin (GoT). This study takes an approach based on two-particles statistics providing
21 the relative dispersion, relative diffusivity and Finite Size Lyapunov Exponent (FSLE) estimates. In the GoT,
22 the relative dispersion follows the predictions from the theory of two-dimensional turbulence with two inertial
23 subranges identified in the kinetic energy spectrum with the spectral slopes $-5/3$ and -3 . The time evolution of
24 dispersion shows an exponential growth during 5 – 8 days, followed by a power law regime during the next 6
25 to 20 days. Fixed-length indicators from the relative diffusivity and the FSLE reveal a local dispersion at large
26 and intermediate scales (above Rossby radius of deformation) and non-local dispersion in sub-mesoscale range
27 (below Rossby radius of deformation). The effect of river runoff on the local hydrodynamics and dispersion
28 processes is assessed using the numerical model simulations without river discharge. The results show that in
29 the model, the river plume, when present, highly impacts the Lagrangian statistics. High gradients of buoyancy
30 reinforce the sub-mesoscale circulation in a large region along the Vietnamese coast and modify the scales and
31 intensity of turbulent dispersion. However, a clear change of dispersion regime in the sub-mesoscale range is
32 not identified, suggesting that the mesoscale circulation in the GoT largely governs particle spreading even at
33 small scale.

34 **Keywords:** Relative dispersion; Scale of motion; HF radar measurements; Numerical modeling; Gulf of
35 Tokin.

36

37 **1. Introduction**

38 Transport and dispersion processes in the ocean have practical importance since they play a major role in the
39 functioning of marine ecosystems by carrying physical and chemical quantities such as heat, salt, nutrients, as
40 well as biological relevant tracers, matter and marine debris. For example, in the North Sea, the transport of
41 the flatfish larvae from the spawning areas to the nurseries and mortality rate are heavily impacted by the
42 hydrodynamics processes and the environmental factors (Lacroix et al., 2013). In the coastal zone, the
43 knowledge of transport properties is even more important for assessing the dispersal of anthropogenic pollutant
44 tracers released accidentally (Corrado et al., 2017). Mapping the transport pathways of materials advected by
45 ocean currents is of great interest for understanding the interconnection between geographical regions (Haza
46 et al., 2010; van Sebille et al. 2011, 2015), physical and relevant biogeochemical processes (d'Ovidio et al.,
47 2015). However, prediction of the Lagrangian transport remains challenging since the oceanic flow is turbulent
48 in a wide range of spatial and temporal scales. The oceanic coherent structures, which we refer to as jets,
49 eddies, fronts, arise from multi-scale interactions of physical processes in the ocean and at its interfaces with
50 the atmosphere and the continent. The instabilities of these structures, due to the flow turbulence or episodic
51 forcing (e.g., wind), result in chaotic motions and may dictate the transport statistics (Haza et al., 2016).

52 Lagrangian framework is naturally linked to the investigation of transport since the Lagrangian observations
53 track the fluid parcels and sample the spatiotemporal evolution of their properties rather than measuring them
54 at a fixed point in the Eulerian approach (Essink et al., 2019). Trajectory maps can provide the details of the
55 circulation and dispersion of materials in the flow field. Since an individual trajectory in the turbulent flow
56 field is largely unpredictable and depends strongly on the initial conditions, the ensemble average over many
57 trajectories is needed to provide the statistical description of the flow field (La Casce et al., 2008; Essink et al.,
58 2019).

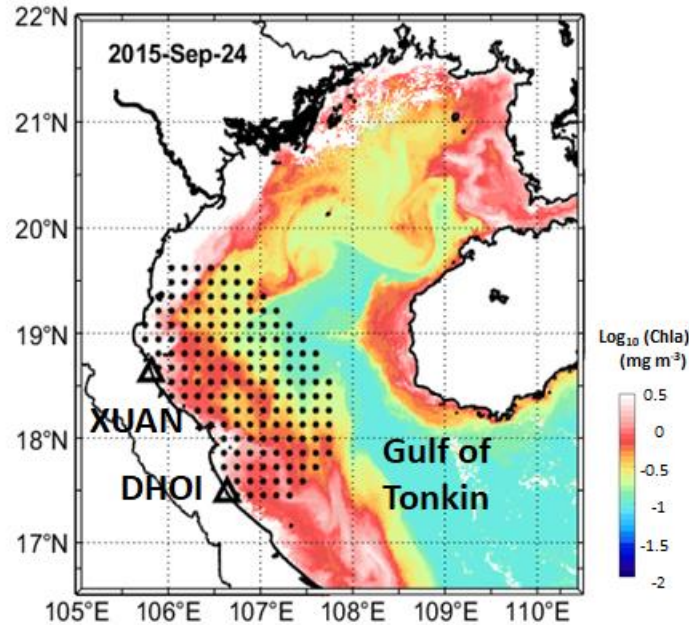
59 Characteristics of the oceanic turbulent flow based on the Lagrangian approach have been described in many
60 studies, e.g., in the North Atlantic (Lumpkin and Elipot, 2010), in the South Atlantic, (Berti et al., 2011), in
61 the Nordic Seas (Koszalka et al., 2009), in the Gulf of Mexico (LaCasce and Ohlmann, 2003; D'Asaro et al.,
62 2018), and in the Mediterranean Sea (Haza et al., 2010; Schroeder et al., 2011, 2012). These studies aimed to
63 explore how pollutants or biological tracers disperse in the marine environment and how the energy is
64 transferred across scales of motion. The relative dispersion, which might be estimated from the mean squared
65 separation of particle pairs, is used to characterize the underlying turbulent flow field. Among the Lagrangian
66 statistics, pair dispersion gains importance since the spreading rate of pairs of particles is sensitive to the
67 amount of energy distribution within different scales. The spreading of particle pairs depends, in principle, on
68 the velocity difference at the length scale corresponding to the pair separation distance (Lumpkin and Elipot,
69 2010). Therefore, the statistics based on relative dispersion are useful for the assessment of mixing in the
70 turbulent flow field at small and intermediate scales and can characterize the most important physical processes
71 controlling the underlying fluid motions (Meyerjürgens et al., 2019).

72 The relationship between the oceanic turbulent flow and the relative dispersion statistics has been extensively
73 discussed (see, e.g., LaCasce, (2008); Foussard et al., (2017); Berti et al., (2021)). It was shown that the
74 dispersion properties can be theoretically predicted from the kinetic energy spectrum, $E(k) \sim k^{-\beta}$, of the
75 underlying flow field. Specifically, the relative dispersion can be either local if $1 < \beta < 3$, or non-local, in the
76 case of $\beta \geq 3$. In a number of studies using the relative dispersion statistics (Koszalka et al. 2009; Lumpkin and
77 Elipot 2010; Poje et al. 2014; van Sebille et al. 2015; Sansón 2016; Beron-Vera and LaCasce 2016; Corrado
78 et al. 2017; Essink et al. 2019), the geographic dependency of the stirring regime is found across different
79 ocean regions. Contradictory results in some regions have been reported revealing a non-local dispersion
80 regime at scales below the Rossby radius of deformation and local dispersion in the same scale range. For
81 example, Meyerjürgens et al. (2019) identified significantly different dispersion regimes in the vicinity of the
82 tidal front in the North Sea. Scaling of the relative dispersion indicated a non-local dispersion regime while
83 the Finite Size Lyapunov Exponent (FSLE) showed a local dispersion. At large spatial scales, the existence of
84 different dispersion regimes was revealed. In some studies (e.g., Schroeder et al. 2011 in the Liguro-Provençal
85 basin), a transition to the diffusive regime was identified, whereas other studies indicated a Richardson-like
86 dispersion, most likely due to the effect of large-scale velocity shear (e.g., LaCasce and Ohlmann 2003 in the
87 Gulf of Mexico). In addition, characterization of the dispersion regime based on the observations from drifting
88 buoys alone is practically difficult and requires many pairs of Lagrangian drifters whose number is always
89 limited in ocean regions. The lack of observations leads to differences in assessment of the dispersion regime
90 in the world oceans (i.e., Haza et al., 2008; Schroeder et al., 2012). Recently, advances in observations of ocean
91 dynamics by remote sensing techniques such as altimetry, coastal radars, etc., and the improvement in the
92 ocean modeling accuracy have opened a new opportunity for assessment of the oceanic dispersion properties
93 (using synthetic drifters).

94 The present study is performed in the Gulf of Tonkin (GoT), a shallow, semi-isolated gulf located in the
95 northwestern part of the South China Sea (Fig. 1). As demonstrated in recent studies, the hydrodynamics in
96 the GoT is controlled by the Asian monsoon system, complex bathymetry and exchanges with the South China
97 Sea at the south and through the Hainan Strait (e.g., Tran et al. 2021; Piton et al., 2021, Rogowski et al., 2019).
98 The freshwater input from the Red River impacts the hydrology and circulation along the Vietnamese coast
99 with a strong seasonality as shown recently for instance by Nguyen-Duy et al. (2021). In coastal and shallow-
100 water seas, a combination of tidal and wind forcing, in conjunction with complex topography, can lead to the
101 formation of sub-mesoscale eddies (e.g., Zimmerman et al., 1981). Additionally, large freshwater discharge
102 enhances the density gradients and can also generate sub-mesoscale motions that play an important role in
103 organizing the flow structures and materials transport.

104 In this work, we employ the realistic, high-resolution numerical model SYMPHONIE and velocity
105 measurements by high-frequency radars to investigate the dispersion properties of the flow field. We adopt an
106 approach based on particle pairs statistics to quantify different scales of the flow field variability and associated
107 dispersion regimes, in the GoT. This article is organized as follows. In section 2, we briefly describe the data
108 and methods used for dispersion quantification. The description of the flow fields during two selected periods

109 is given in section 3. In section 4, results of the assessment of the turbulent dispersion based on the coastal
110 radar velocity measurements and the numerical model simulations are presented. We also assess the effect of
111 river discharge on the Lagrangian statistics. We discuss the results in section 5 and summarize them in section
112 6.



113
114 Figure 1: Location of the Gulf of Tonkin. Radar sites providing the data used for the present analyses are
115 indicated by triangles. Black dots indicate the HF radar coverage. The dot spacing is 12 km. Color shading
116 represents a snapshot of the Chl-a concentrations (in \log_{10} scale) obtained from Aqua/MODIS on September
117 24, 2015. Extension of high Chl-a concentration patterns from the nearshore blooming region seaward is
118 visible through the elongated filaments and small eddies.

119 2. Materials and methods

120 2.1. HF radar velocity measurements

121 A coastal radar network, which consists of three radar sites Hon Dau Island (HNDU, 106.81°E, 20.67°N),
122 Nghi Xuan (XUAN, 105.82 °E, 18.62 °N), and Dong Hoi (DHOI, 106.64 °E, 17.47 °N), has been operating
123 within the GoT since 2012 (Fig. 1). The radar network was configured to operate at a frequency of 4.625 MHz
124 (which was changed to 5.25 MHz in 2018). The radial velocity component is measured by the radars at the
125 effective depth of ~ 2 m with an instrumental error of ~ 0.07 m s^{-1} . The following configuration has been used
126 at each radar site to retrieve the radial velocities of the surface currents: 5.8 km along the beam and azimuthal
127 spacing 5° . The temporal resolution was set to 1 h. The surface HFR total velocities were mapped using
128 EOF/Variational interpolation methods (Yaremchuck and Sentchev et al., 2011). The resulting product consists
129 of hourly maps of the two current components (zonal and meridional) on a regular 6-km grid as described in

130 Tran et al. (2021). The data from the HNDU site were not used because of the hardware failures during the
131 study period in 2015.

132 **2.2. Numerical model configuration**

133 We use the numerical simulations of Nguyen-Duy et al. (2021) made with SYMPHONIE model.
134 SYMPHONIE is a hydrostatic, numerical model which solves the primitive equations on a curvilinear bipolar
135 Arakawa C-grid with regular sigma vertical levels (Marsaleix et al., 2006, 2008). A description of the model
136 and of the configuration is given in Nguyen-Duy et al. (2021) and we only recall here the characteristics
137 relevant to this study. The grid covers the whole GoT with a highly variable horizontal resolution, from ~300
138 m near the Red River delta to ~4500 m near the open boundaries. The water column is discretized onto 20
139 sigma levels. The bathymetry is reconstructed from GEBCO 2014 combined with other sources and field
140 surveys in order to characterize the complex topography, with many islands and islets located within the region
141 and especially the coastal area adjacent to the Red River delta (Piton et al., 2019). Intertidal areas are simulated
142 with a wetting and drying scheme. The k- ϵ turbulence closure scheme is implemented as in Michaud et al.
143 (2012).

144 Tidal motions at the open boundaries are prescribed from the sea surface elevation and barotropic currents of
145 9 tidal constituents from the FES2014 atlas (Lyard et al., 2021). The tidal astronomical potential is also
146 considered at every grid point of the model. In addition, the 1/12° spatial resolution, daily averaged sea surface
147 height (SSH), velocity components temperature, and salinity provided by the Copernicus Marine Systems
148 (CMEMS) global model are also used at the boundaries.

149 At the sea surface, the boundary conditions include the 3-hourly data for wind, precipitation, solar energy,
150 atmospheric temperature and pressure from the Operational ECMWF product. The fluxes of momentum, heat,
151 and freshwater are computed internally in the model using the bulk formulae of Large and Yeager (2004).

152 In the reference simulation (hereafter GoT-Ref) the river discharge from 16 rivers is introduced in the model
153 and configured as realistically as possible according to the method described in Nguyen-Duy et al. (2021).
154 Daily freshwater runoff is used from the main seven distributaries of the Red River. For other rivers,
155 climatological data are used. An additional configuration without the river discharge (GoT-noriv configuration,
156 see Nguyen-Duy et al., 2021) is used to assess the effect of rivers discharge on the dispersion properties.

157 The model was extensively validated over the period 2011-2016 and the results of the validation are given in
158 Piton et al. (2021) and Nguyen-Duy et al. (2021). In our study, we performed an additional comparison of the
159 model simulation with the current velocity derived from HFR measurements for two periods (August and
160 November 2015, Fig. 2). The correlation between the current velocity derived from both data sources remains
161 larger than 0.7 with a slightly higher value obtained in November (0.85). A relative difference of about 6-10%
162 quantifies the disagreement between the HFR data and the numerical simulations, for both the latitudinal (u)
163 and longitudinal (v) velocity components. The model velocities were found to be slightly smaller than those
164 derived from HFR measurements.

165 2.3. Lagrangian diagnostics

166 In this study, we used the velocity data from the model simulation covering one-year long period in 2015.
167 Virtual particles organized in clusters were advected using oceanParcels Lagrangian framework
168 (<https://oceanparcels.org>) by the velocity field from the model at one hour resolution. These Lagrangian
169 tracers, with a total number of 24065 particles, were uniformly distributed in the surface layer at 2 m depth.
170 Each cluster included one center particle and two satellite pairs along x- (longitude) and y-axis (latitude) with
171 the initial separation $\delta_0 = 0.5$ km. The clusters were seeded every 2 km across the domain in order to keep the
172 initial pair separation as low as possible and to not exceed a reasonable computational cost. The particles are
173 advected horizontally using the 4th order Runge-Kutta scheme.

174 In this study, we focus on assessing the statistics of Lagrangian particle pairs advected in the flow fields derived
175 from the HFR measurements and the model simulation during two seasons (summer and late fall). The
176 Lagrangian quantities analyzed include relative dispersion, relative diffusivity and Finite Size Lyapunov
177 Exponent (FSLE).

178 Relative dispersion is a common metric for assessing the dispersion of tracers. It is defined as the average,
179 over all particle pairs, of the squared separation between particles i and j in a pair at time t :

$$180 \quad \delta^2(t) = \frac{1}{N(N-1)} \sum_{ij}^N \|\vec{x}_i(t) - \vec{x}_j(t)\|^2, \quad (1)$$

181 where N is the number of particles. The pairs were identified using the particles with initial separations below
182 2 km. The relative dispersion behavior depends on the level of turbulence in the flow field. The latter is
183 reflected in the kinetic energy spectrum which shows a power law distribution as a function of the (horizontal)
184 wavenumber $k=|\vec{k}|$: $E(k) \simeq k^{-\beta}$. At the early stage when the pair separation is small, the particle pair velocities
185 are close and the growth of relative dispersion follows a ballistic behavior, $\delta^2 \sim t^2$. At larger times, relative
186 dispersion grows exponentially in the case of non-local dispersion, when $\beta > 3$. Otherwise, if $1 < \beta < 3$, relative
187 dispersion is local and scales as a power law $\delta^2 \simeq t^{\frac{4}{3-\beta}}$ (Foussard et al., 2017). Richardson super diffusive
188 regime corresponds to $\delta^2 \sim t^3$ where the pair separation is controlled by eddies with a size similar to the
189 separation distance of particles. When the particle separation reaches scales much larger than the largest
190 characteristic flow scale, the pair velocities are considered uncorrelated. Relative dispersion in this case is
191 expected to scale as $\delta^2 \simeq t$, corresponding to a diffusive behavior.

192 In addition, we diagnose the relative diffusivity κ , which represents the growth rate of the average squared
193 separation. This quantity is defined as the time derivative of relative dispersion,

$$194 \quad \kappa = \frac{1}{2} \frac{d\langle \delta^2(t) \rangle}{dt}, \quad (2)$$

195 and it can be useful to assess the mixing properties and the corresponding spreading regime. For this purpose,
196 it is often interesting to consider κ as a function of the separation distance δ , rather than of time. Depending on

197 the shape of the given kinetic energy spectrum, $\kappa(\delta)$ scales as δ^2 for the non-local dispersion regime and as $\delta^{4/3}$
198 (when $\beta=5/3$) for the local dispersion one.

199 The third quantity, the Finite Size Lyapunov Exponent (FSLE), is estimated by measuring the time τ , averaged
200 over all particle pairs, needed to separate particles in a pair from a distance δ_k to a distance $\delta_{k+l} = r \delta_k$, with r
201 > 1 ($k=1, N_k$ and N_k is the number of pairs chosen in a way to span the relevant range of scales):

$$202 \quad \lambda = \frac{\ln(r)}{\tau} \quad (3)$$

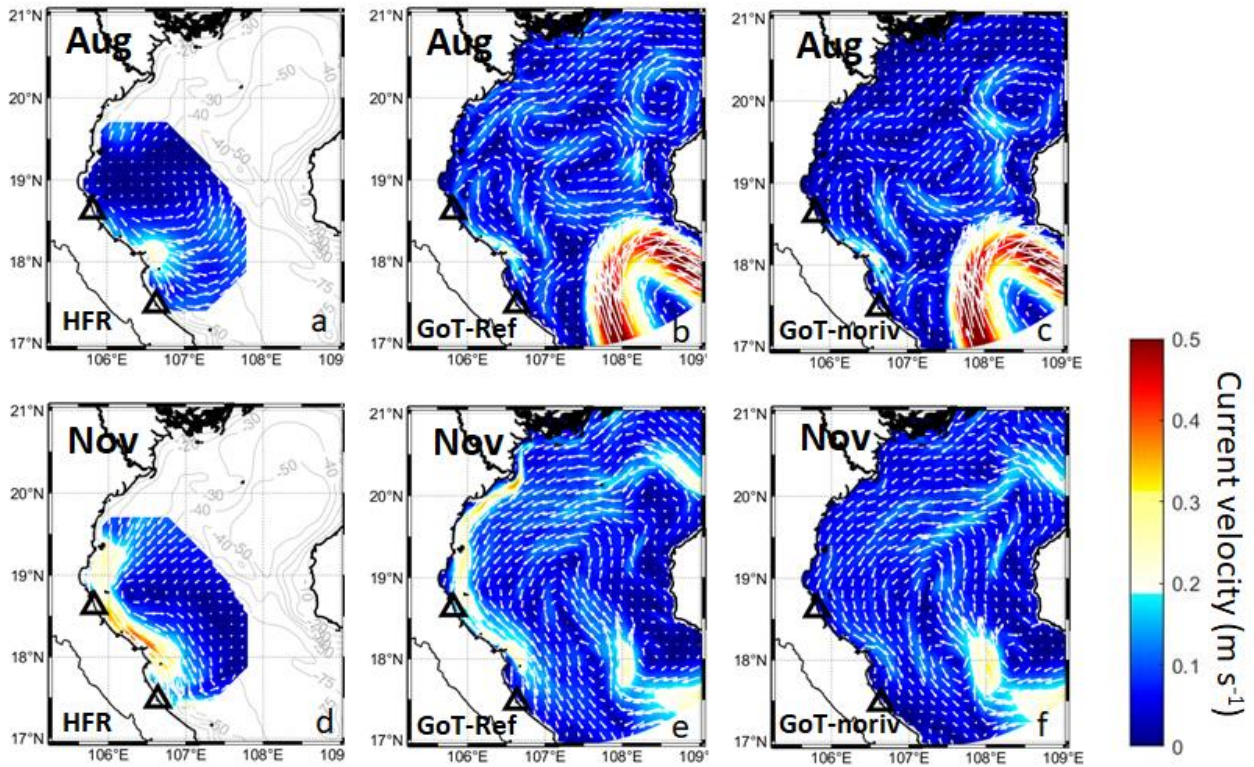
203 Values of FSLE can be used to distinguish a local regime of dispersion from a non-local one (Schroeder et al.,
204 2011). Compared to relative dispersion, the FSLE, being a fixed-length (instead of fixed-time) indicator, better
205 allows to disentangle contributions from turbulent features of different size (Artale et al., 1997). We
206 implemented a method called fastest-crossing for the computation of the FSLE (Lumpkin & Elliot, 2010). A
207 sensitivity study of the results to the choice of r was performed with the fixed number of particles in the area.
208 It was found that varying r from 1.2 to 1.6 does not change the FSLE slope considerably (Poje et al., 2014)
209 and the value of $r = 1.4$ was chosen. The Lyapunov exponent quantifies the exponential rate of separation and
210 is often used for the identification of the nonlocal regime of pair separation (Haller & Yuan, 2000). At very
211 small separations, the FSLE is expected to recover such, scale-independent, value. The behavior of the FSLE
212 in a turbulent flow field with spectrum $E(k) = k^{-5/3}$ typically is as follows: $\lambda \simeq \text{constant}$ (exponential growth
213 and nonlocal dispersion regime) at very small scales, $\lambda \simeq \delta^{-2/3}$ for local dispersion (Richardson regime) in
214 the inertial range and $\lambda \simeq \delta^{-2}$ for the diffusive regime expected at separations much larger than the largest
215 flow scales (Berti et al., 2011; Corrado et al., 2017). A ballistic regime $\lambda \sim \delta^{-1}$ can also be expected in the
216 presence of intense mean currents.

217 **2.4. Horizontal stirring from FSLE maps**

218 In addition, the spatial distribution of FSLEs has been obtained for two selected periods representing two
219 seasons (in August and November). The backward FSLE calculations were performed for 30 days with a
220 timestep of 1 hour, following the method proposed by d'Ovidio et al. (2004). The advantage of this technique
221 is to restrict the analysis of dispersion within relevant structures among selected length scales. The optimum
222 choice for the spatial FSLE amplification factor δ_f/δ_i was discussed several times in previous studies (Haza
223 et al., 2010; Berta et al., 2014). We compute the exponential growth rate, $\lambda(x)$:

$$224 \quad \lambda(x) = \frac{1}{\tau(x)} \ln \left(\frac{\delta_f}{\delta_i} \right) \quad (4)$$

225 in analogy with Eq. (3), with $\delta_i \simeq 1.86$ km and $\delta_f = 13$ km. Such values of δ_i and δ_f allow to adequately
226 visualize the relevant coherent structures and transport patterns associated with small-scale processes.

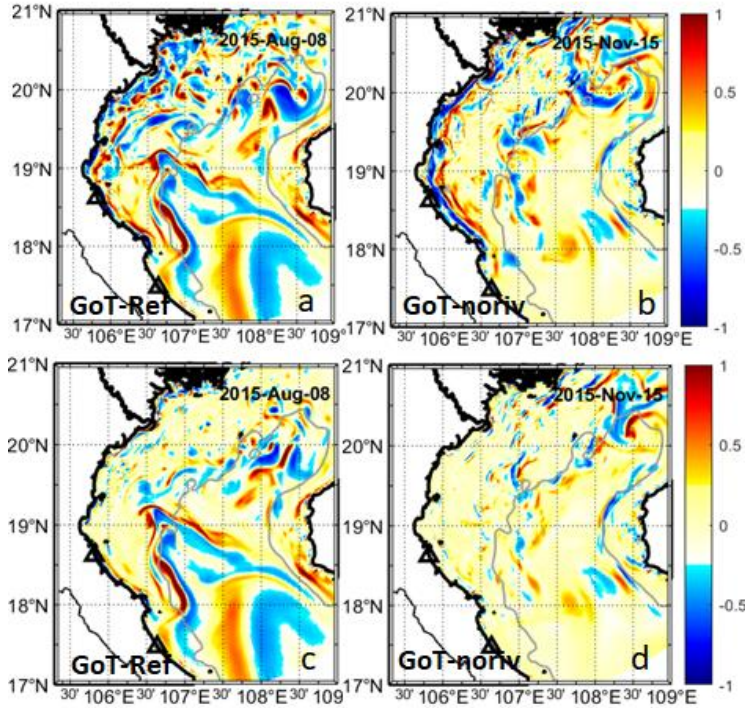


227

228 Figure 2: 30-day mean surface currents in the GoT from HFR (a, d) and numerical model in two
 229 configurations: with river discharge (b, e) and without river discharge (c, f) in August and November 2015.
 230 The current vectors are interpolated on a regular grid and plotted every 15 km.

231 **3. Description of the Eulerian flow fields**

232 Figure 2 shows the 30-days averaged surface current fields from the HF radar measurements and from model
 233 simulations in August and November (Fig. 2). During summer, the prevailing wind is from the southwest
 234 direction and remains persistent until September 12 when a typhoon hit the region. Interestingly, during
 235 August, the surface currents from the model show a pronounced northeast flow in the northern part of the gulf
 236 above 19°N which roughly follows the 50m isobath. This flow is partly captured in the northern part of the
 237 radar field (Fig. 2a). During November, the wind changes to northeasterly with larger speed. The surface
 238 currents demonstrate a typical winter pattern with a gulf-scale cyclonic circulation, an intense coastal current
 239 in the western part (Fig. 2 d, e), and several energetic jets with mean velocity of 0.3 m s^{-1} . The lack of river
 240 discharge in the model leads to decrease surface current velocity (by roughly 0.1 m s^{-1}) in the vicinity of the
 241 Red river mouth in August (Fig. 2b, c) and large reduction of the southward coastal jet in November (Fig. 2f).



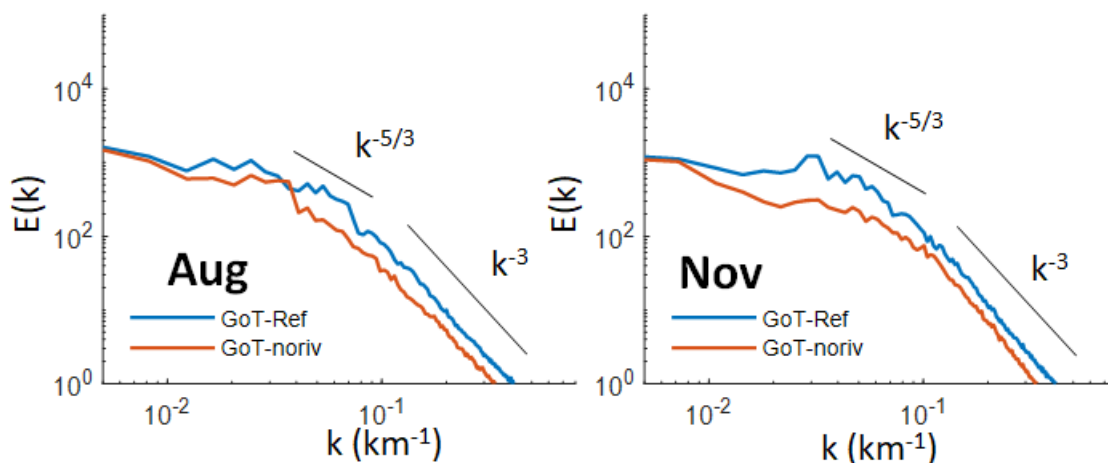
242

243 Figure 3: Snapshots of the relative vorticity normalized by Coriolis frequency in August and November 2015
 244 from model simulation with (a, c) and without river discharge (b, d). Gray line shows 50 m isobath.

245 While the mean current patterns look similar for three velocity fields, some significant differences appear when
 246 considering the gradient of the flow field, e.g., the relative vorticity, $\zeta = \frac{\partial v}{\partial x} - \frac{\partial u}{\partial y}$, which controls the separation
 247 process of the advected Lagrangian particles. Fig.3 shows snapshots of the relative vorticity ζ normalized by
 248 the Coriolis frequency f from the model simulations. It indicates that the dynamics of the GoT in both periods
 249 is dominated by a wide range of motions, from a large-scale structure induced by the incoming current from
 250 the open-sea that occupies the southern area in August (Fig. 3b) to abundant thin filaments and small vortices
 251 across the gulf of the size from few to tens of km and with magnitude as large as $(1-1.5)f$ (Fig. 3a, c). When
 252 the Rossby number $R_o = \zeta/f \sim O(1)$, a departure from the geostrophic equilibrium in the flow is expected and
 253 smaller-scale processes can come into play, such as frontogenesis, mixed-layer instability (Zhong and Bracco,
 254 2013). Consequently, these sub-mesoscale structures of the velocity fields can directly impact the dispersion
 255 process by increasing the rate of dispersion by an order of magnitude compared to the geostrophic turbulence
 256 (Berta et al., 2020). A significant difference in velocity gradients between the full model and the model without
 257 river discharge is the lack of a number of structures with high vorticity which are observed better in the vicinity
 258 of the Red river mouth in August and in November (Fig. 3b, d). Due to the coarse resolution of the HFR
 259 measurements, the vorticity field is much smoother, its magnitude is drastically reduced, and small-scale
 260 coherent structures are almost vanishing (results not shown).

261 The statistical characterization of the velocity field variability can be obtained from the surface turbulent
 262 kinetic energy spectrum, $E(k)$ (Fig. 4). The spectra indicate a wide range of motions: from geostrophic and
 263 wind driven circulation at large scale to sub-mesoscale turbulent motions. The energy distribution appears

264 different between two periods and higher for the GoT-Ref model configuration than for the GoT-noriv case.
 265 In both models, the kinetic energy is concentrated at large scales (roughly at the length scale about 60 km) and
 266 decays more rapidly (steeper spectral slope $\sim k^{-3}$) at scales below 20 km. In the range roughly above 20 km,
 267 despite some noise, the energy distribution follows $k^{-5/3}$ law in both seasons. While the difference in energy
 268 distribution between two seasons is rather small, a significant difference is observed for model simulations
 269 with and without rivers forcing. In the latter case, the spectral slope from GoT-noriv model in summer appears
 270 steeper in a wide range of scales, 8 – 70 km, indicating a nonlocal dispersion regime from a Lagrangian
 271 perspective (Fig. 4a) while in November, above the range 10 – 30 km, the dispersion regime seems foster the
 272 local dispersion (Fig. 4b).



273
 274 Figure 4: Power spectra of surface horizontal turbulent kinetic energy in August (a) and November (b) for
 275 two model configurations: with and without river input.

276 4. Lagrangian pair dispersion

277 4.1. Lagrangian dispersion from HFR measurements and model simulation

278 In order to assess the turbulent dispersion in the vicinity of the Vietnamese coast, a first Lagrangian tracking
 279 experiment was conducted. A total of 2800 particles were uniformly seeded in a rectangular area of the size
 280 30 x 30 km². Fig. 5 (right panel) shows the trajectories of particles advected in the velocity field derived from
 281 HFR measurements. For comparison, those of particles advected by the model velocity field are shown in the
 282 left panels of the same figure. The drifting time of each particle is shown in color. Two releases were
 283 performed, one on August 3 and another on November 10, with a tracking time of 30 days. During the first
 284 tracking period, the surface currents are driven by the southwest monsoon while during the second period, the
 285 winter cyclonic circulation is formed, and the coastal current is reinforced as described in the previous section.
 286 For particles released in August, trajectories are globally controlled by the cyclonic eddy located at the latitude
 287 19°N which “trapped” the particles during the first 10 days. The effect of particle trapping is clearly seen in
 288 trajectories drawn in the model and radar velocity fields (Fig. 5a, b). Ten days after the release when the eddy
 289 is weakened, particles separate in different directions in the model simulations. One group of them remains

290 within the coastal zone close to XUAN radar site while another group is transported by the coastal buoyant jet
291 southward, down to the gulf entrance (Fig. 5a). The direction of particle advection in the radar-derived velocity
292 field is also southward for days 10 to 20, then it changes to eastward and northward (Fig. 5b). Agreement
293 between the two transport patterns is found only for the first 15 to 20 days of tracking.

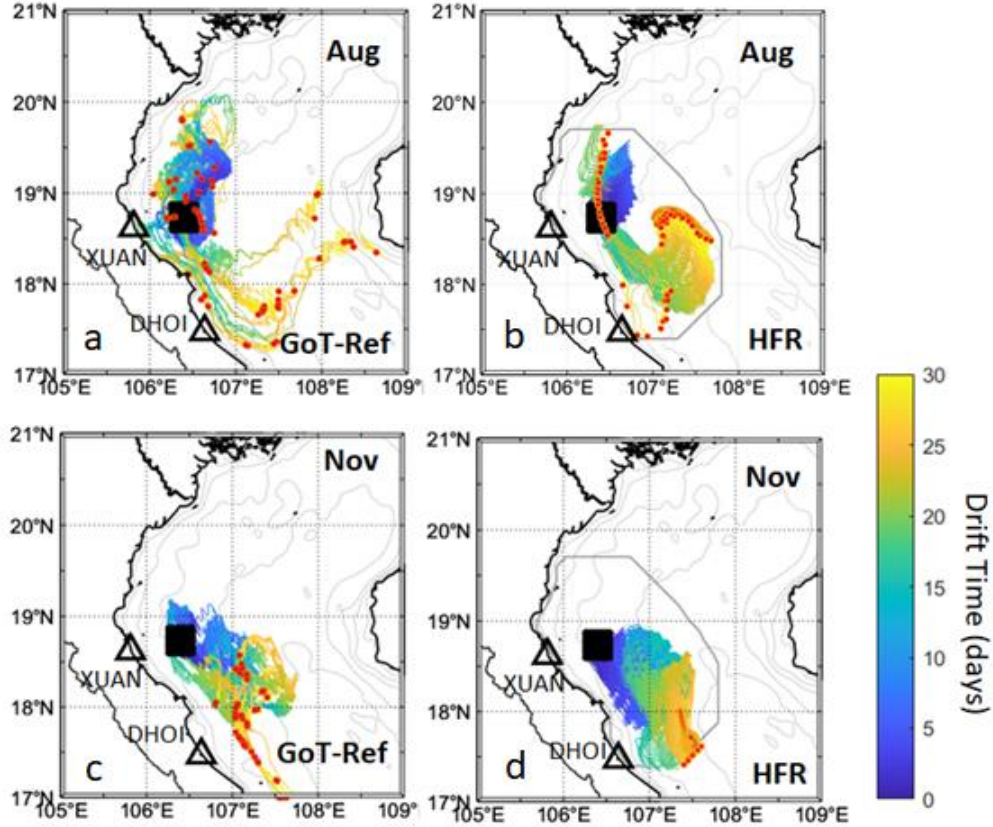
294 In November, a much better agreement in advection pathways in both HFR-derived and model velocity fields
295 is found. In both cases, the trajectories of particles are related to the cyclonic circulation responsible for their
296 transport southward. At the early stages, most of the particles are advected southward by the coastal jet. Later
297 in time (roughly 10 days after the release), the particle drift direction changed to offshore, then reversed to
298 northward after 15 days before continuing to the south after day 20. Regarding the number of particles
299 remaining within the radar coverage area, 30% of particles left the area covered by HF radar measurements
300 while this number is 10% for particles advected by the model velocity fields. The final location of the particles
301 is shown in Fig. 5 in red color. At the end of the 30 days period, the particles advected in the radar velocity
302 field show a more uniform distribution, while in the model simulation, the particles are separated into a number
303 of different groups (Fig. 5). It is possible that larger dispersion in the model simulation is caused by
304 irregularities in velocity fields due to sub-mesoscale motions which are probably resolved in the high-
305 resolution model.

306 To quantify the dispersion regime, we used relative dispersion and the FSLE. In the subsequent analysis of the
307 turbulent dispersion, we used the estimation of the Rossby radius R_d performed by Nguyen-Duy et al. (2021).
308 In summer (April to September), large river discharge and thermal exchange with the atmosphere lead to the
309 increase of stratification and R_d ranges from 10 to 15 km. During winter (Oct to Mar), strong wind and waves
310 increase mixing in the water column. As a consequence, R_d has values of about 4 to 8 km and is even smaller
311 in the shallow water area (see Fig. 4 in Nguyen-Duy et al., 2021). Therefore, in this study, the value of 8 km
312 in November and 15 km in August are adopted for R_d .

313 Despite the differences in advection pathways, the relative dispersion regimes appear rather similar (Fig. 6).
314 For the cluster released in August, for both radar and model fields, relative dispersions indicate an exponential
315 regime ($\exp(0.8t)$) occurring during the first 10 days. It should be noted that in the case of the radar field, the
316 pair separation grows slowly during the first 3 days, which can be explained by the coarser resolution of the
317 HFR measurements (~ 6 km) that is larger than the initial separation (~ 2 km). During the next few days, the
318 dispersion rapidly increases until reaching the distance equal to the grid resolution. The similarity in the
319 exponential growth shown in Fig. 6a for both the HFR and the model indicates that relative dispersion during
320 this initial period is dominated by processes with length-scale larger than the pair separation distance. On day
321 15, both curves flatten, suggesting that the particle pairs possibly reached eddies with typical length scale of
322 about (20-30) km and larger (at later times). The evolution of relative dispersion follows a power-law behavior
323 not far from Richardson regime for the model ($\delta^2 \sim t^3$) and ballistic regime for the radar ($\delta^2 \sim t^2$). The latter
324 result is affected by larger statistical errors (Fig. 6a).

325 In November, the relative dispersion shows larger differences (Fig. 6b). Although the particles were released
326 at the coastal current boundary which can rapidly separate the particles pairs, only the model indicates a high

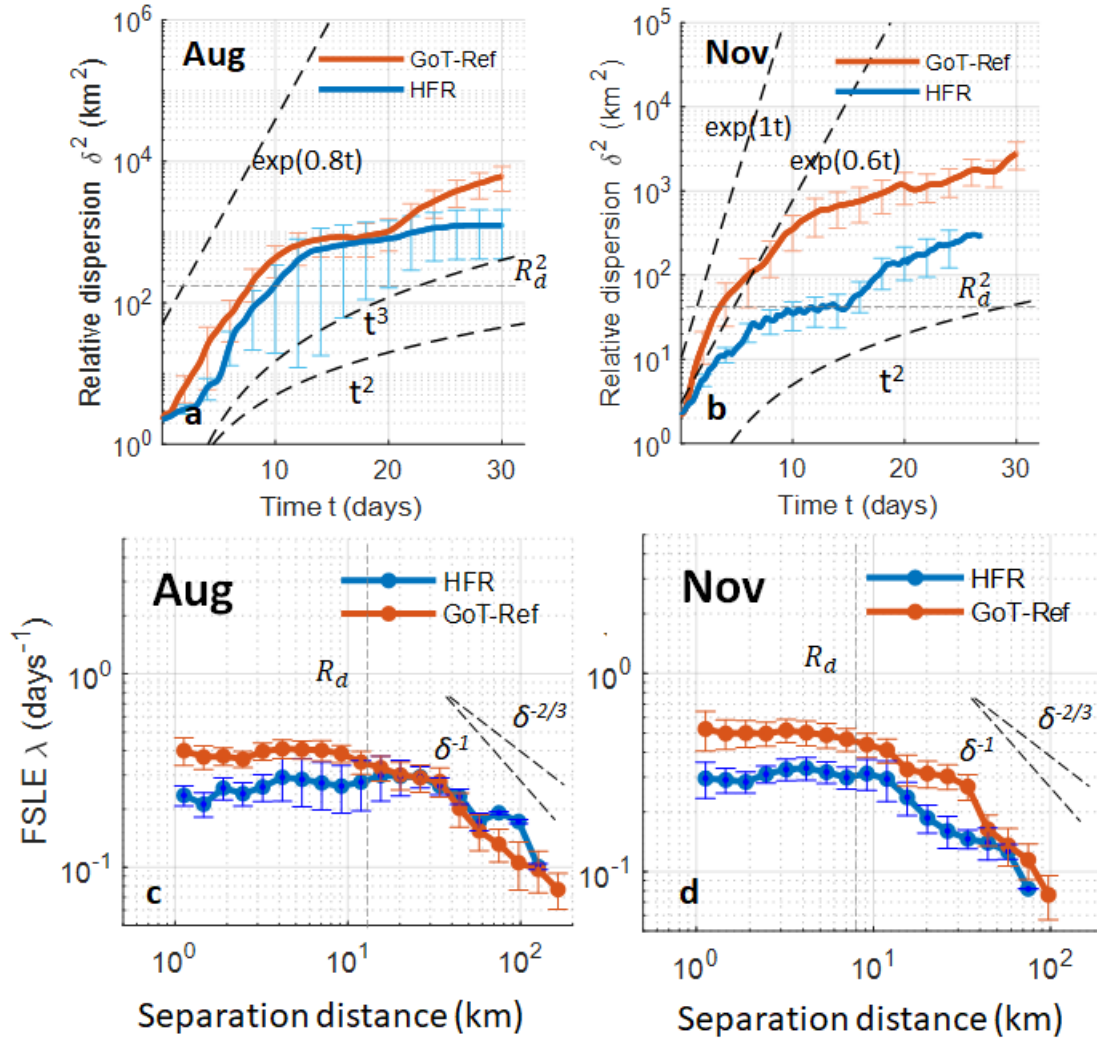
327 rate of exponential growth ($\exp(t)$). This exponential phase is short, and last approximately 4 days. Compared
 328 to the model, the exponential growth in the HFR measurement is lower. After 10 to 15 days, both curves
 329 display a separation growth that is intermediate between a ballistic (t^2) and Richardson (t^3) regime, although
 330 it is more difficult to characterize the growth law for the HFR-derived data.



331
 332 Figure 5: Trajectories of the subset of particles released close to the XUAN radar site (black squares) during
 333 both periods of study from the model (left panel) and from the HFR data (right panel) for 30 days since
 334 release. The drift time is color-coded. The particle final positions correspond to the red points.

335 Another approach used for identification of dispersion regimes involves the FSLE analysis (Fig. 6c, d). The
 336 FSLE uses the pair separation distance as an independent variable, thus, it is less affected by the superposition
 337 of contribution from pairs evolving under different dispersion regimes at the same time. In agreement with
 338 relative dispersion, the FSLE curves demonstrate a non-local dispersion regime for the scale range below 10
 339 km, where the FSLE is constant, $\lambda(\delta) \approx \lambda_L$, with λ_L the maximum Lagrangian Lyapunov exponent (Fig. 6c,
 340 d). In this range, the associated e-folding time ($T = 1/(2\lambda_L)$) is close to the values found in Fig. 6a, b, i.e.,
 341 from 1 to 1.25 days in the model and from 1.25 – 1.6 days in the HFR velocity fields. The increase in
 342 exponential growth rate in correspondence with increased grid resolution (model vs HFR data) is consistent
 343 with previous works (Poje et al., 2010) as pair dispersion at small separation is affected by small-scale motions
 344 resolved by the model.

345 At larger scales, somewhat common behavior can be recognized. In August, a transition of the dispersion
 346 regime is observed at the scale of about 30 km. Above this scale, the FSLE indicates a regime of dispersion
 347 close to Richardson one ($\lambda(\delta) \sim \delta^{-2/3}$) for both velocity fields. A similar change of dispersion behavior is
 348 observed in November, but now at a scale of roughly 10 km, beyond which the FSLE is somehow steeper than
 349 Richardson regime and approaches the scaling ($\lambda(\delta) \sim \delta^{-1}$) typical of a ballistic regime.



350
 351 Figure 6: Scaling properties from relative dispersion (a, b) and FSLE (c, d) for particles advected by model
 352 and HFR-derived velocity field in August and November. The horizontal (a, b) and vertical (c, d) lines
 353 correspond to separation distances equal to the Rossby radius R_d .

354 4.2. Transport and dispersion of particles in the GoT from model simulations

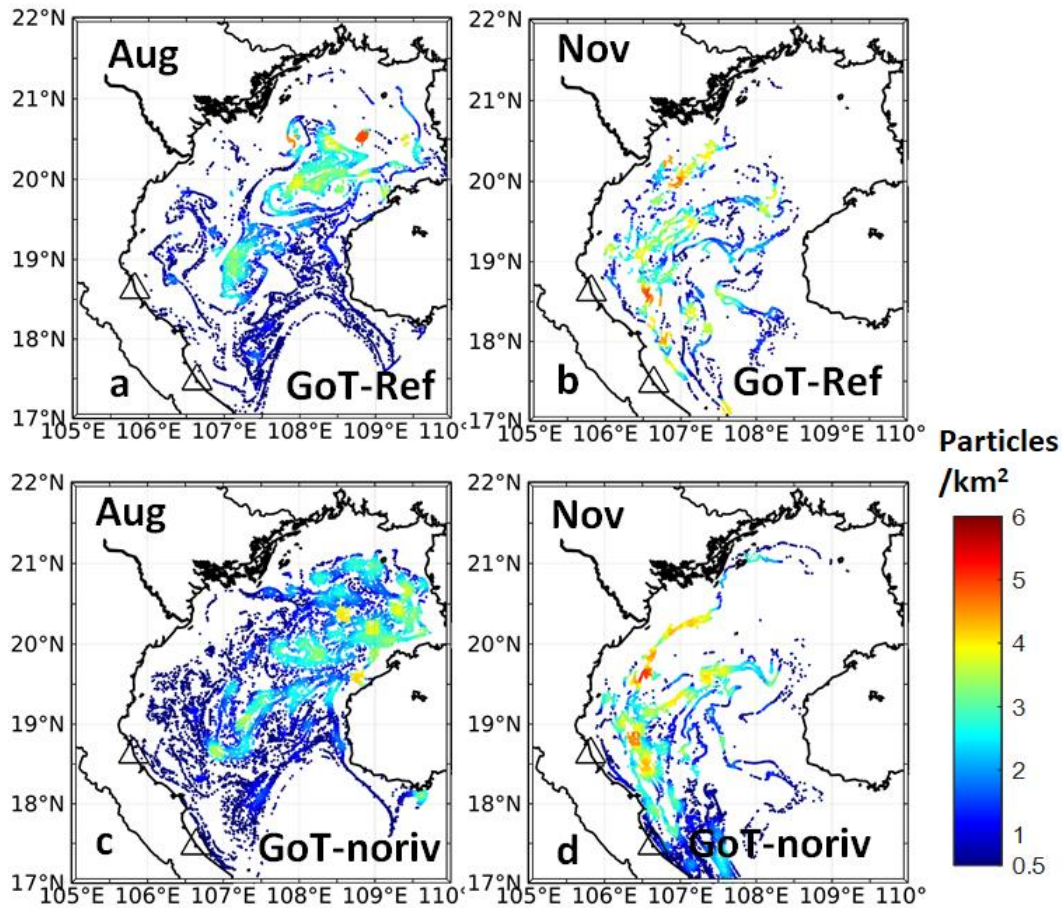
355 Beside the coarse resolution of the HFR-derived velocity field, another weakness of the HFR measurements is
 356 the limited coverage which prevents the assessment of dispersion properties in an area in which the dynamics
 357 are strongly dominated by large-scale circulation features (gulf-scale eddy, coastal jet, etc.). Thus, to extend
 358 the study area to the whole region, we resort to numerical simulations. In particular, we are interested in
 359 assessing the effect of the river discharge which can rapidly generate sub-mesoscale structures and largely

360 affect the dispersion in the small-scale range. A series of Lagrangian tracking experiments were performed
361 during the same two periods (August and November) with particles seeded uniformly in the whole domain of
362 model simulation. The average density of particle distribution at the release is 1.25 particles/km². Two model
363 configurations were used to assess the Lagrangian transport: the model with all forcings including the river
364 discharge (GoT-Ref) and without river discharge (GoT-noriv). Fig. 7 shows the spatial distribution of particles
365 30 days after the release on August 3 (a, c) and November 10 (c, d) and their concentration per km². In all
366 cases, the spatial distribution of particles is found to be controlled by the flow field forced by the monsoon
367 system. The particle distribution reveals a large difference between seasons. In August, the synthetic drifters
368 are scattered throughout the gulf with a high density of particles observed in the middle and the northern gulf,
369 while in November, most of the particles are located in the western gulf (Fig. 7b, d). At the end of the 30-day
370 period, roughly 75% and 90% of particles released in August and November, respectively, remain inside the
371 gulf. This suggests that the hydrodynamics of the gulf is quite local and the exchange with the open sea is
372 limited. The number of particles leaving the domain is likely impacted by the open-boundary conditions. This
373 effect will be evaluated in further studies.

374 Regarding the impact of the river discharge, the model simulation revealed that the distribution in August is
375 quite similar in the southern gulf, whose dynamics are dominated by the inflow through the southern boundary
376 (Fig. 7a, c). A much larger difference can be seen in the northern gulf. In the GoT-Ref case, the particles are
377 organized into long filaments and wrapped around different eddies. Two regions of high particle density of
378 particles are found there. The shape of the particle spatial distribution mimics the eddy-like structures with
379 sizes that can reach 100 km. In the GoT-noriv case, the particle distribution is characterized by more disorder
380 and homogenous scattering across the northern gulf. In general, the particle distribution in August reveals that
381 mesoscale motions are largely enhanced by the river discharge which increase the number of well-organized
382 structures characterized by higher concentrations of particles.

383 In November, both models show a large number of elongated structures in particle distribution field. These
384 structures are associated with the unstable manifolds (attracting the materials drifting with currents) and thus
385 structuring the transport of particles. They also indicate a cyclonic pattern in the GoT winter circulation (Fig.
386 7b, d). Moreover, the particle distribution in both model simulations shows higher concentrations along the
387 middle Vietnamese coast, between 18° – 20° N. In the GoT-Ref case, the lines of high-density particle
388 distribution extend toward the south, demonstrating a tendency of particle alignment along the outer edge of
389 the coastal current that carries them southward. In addition to the rapid southward transport, the fluctuation of
390 the jet can facilitate the formation of eddies at the jet boundary, as described via idealized model (Poje et al.,
391 2010) which contribute to the enhancement of particle spreading.

392 In the GoT-noriv case, the majority of particles are concentrated along a line located roughly 50 km offshore
393 in the northern part and in the southwestern part of the gulf, with large density (~5 particles per km²) observed
394 in the vicinity of the shoreline between latitudes 18°N and 19°N (Fig. 7d).



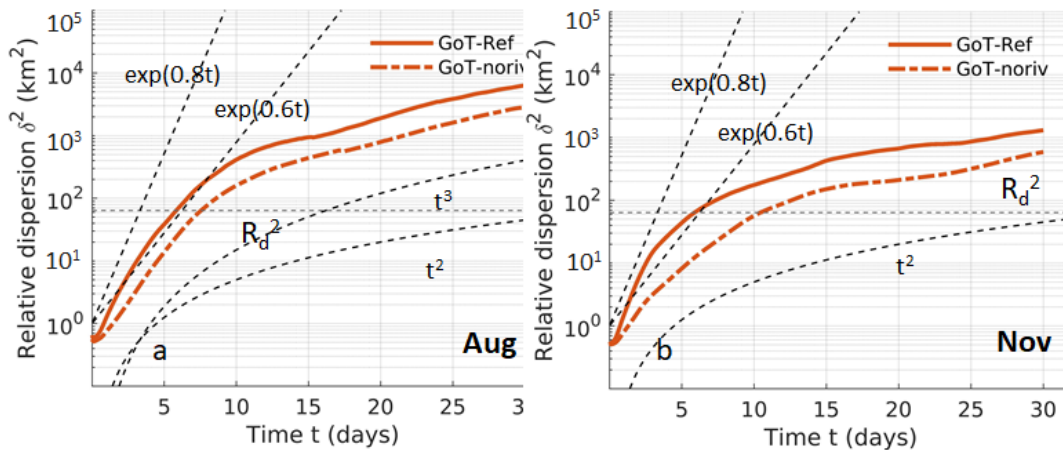
395
 396 Figure 7: Particle distribution in August and November 30 days after the release from the full model (GoT-
 397 Ref) (a, b) and without river discharge (GoT-noriv) (c, d) (unit: number of particles per km²)

398 Fig. 8 helps to characterize the relative dispersion regime in the GoT during the two periods of interest. In
 399 August, relative dispersion shows an exponential regime $\exp(0.8t)$ in the GoT-Ref case while it grows a bit
 400 more slowly in the GoT-noriv case ($\sim \exp(0.6t)$) (Fig. 8a). A change in dispersion regime occurs after 8 days
 401 when the average squared separation exceeds 8 km, a scale close to R_d . The exponential regime indicates non-
 402 local dispersion which can be expected at sufficiently small scales, where the flow is smooth. In our case, the
 403 separation ($\delta \sim 10$ km) at which dispersion changes behavior is larger than the model resolution. This suggests
 404 that dispersion is driven by eddies of larger size at least, namely of $O(R_d)$. At intermediate times, roughly
 405 from 10 days onward, relative dispersion displays a power-law dependency close to a local Richardson regime
 406 ($\delta^2 \sim t^3$) at scales larger than 40 km (Fig. 8a).

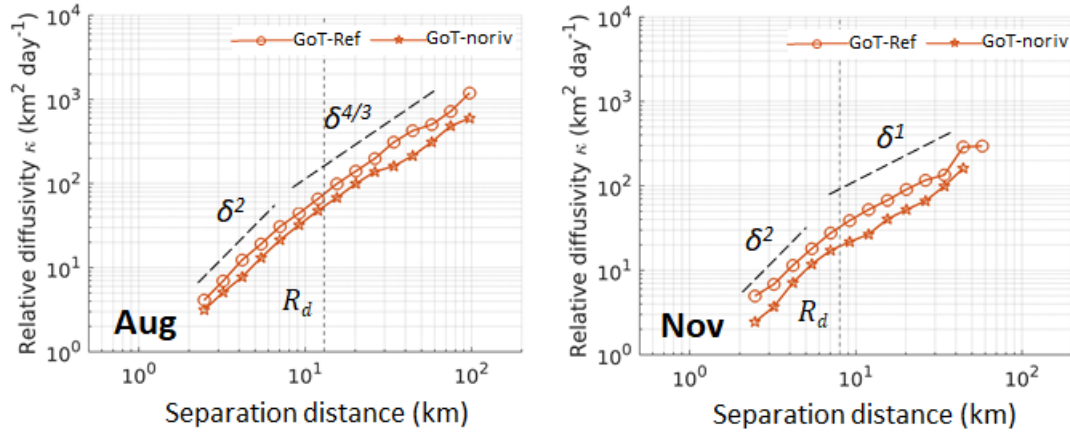
407 In November, exponential growth in the GoT-Ref case with a similar rate occurs for a shorter timescale of 3
 408 days (Fig. 8b) then quickly changes to a regime closer to the ballistic ($\delta^2 \sim t^2$) than to Richardson ($\delta^2 \sim t^3$),
 409 hinting to particles separating due to the coastal buoyant jet. The ballistic regime holds until the end of the
 410 tracking period, when the largest separation of roughly 30 km is reached. The estimated slope for this period
 411 is 2.2. In the GoT-noriv case, exponential growth is observed in a short early period, but with a
 412 smaller rate ($\sim \exp(0.6t)$). The general features of the evolution of dispersion are not very different from those
 413 of the previous cases. The ballistic regime occurs after 5 days of drift. A possible explanation for the change

414 to the ballistic regime in both configurations seems to be related to the particle entrainment inside the coastal
 415 current where the velocity shear causes a rapid separation in the cross-jet direction. In the whole, the rate of
 416 dispersion in the GoT-Ref case appears larger than that in the GoT-noriv simulation. The difference is caused
 417 by the presence of fine motions generated by the river plume advection where particles are stirred more
 418 effectively in the area that is not controlled by the mesoscale motions.

419 Fig. 9 shows relative diffusivity κ as a function of the separation distance δ in August and November
 420 respectively. The variability of this quantity is more affected by noise as κ is the time-derivative of relative
 421 dispersion. Thus, following Koszalka et al. (2009), we binned $\kappa(\delta)$ in such a way that a given value of δ is a
 422 multiple of the previous one, as one would do for the computation of the FSLE. Only the values with more
 423 than 50 data points for each bin are considered in the analysis. Despite some wiggles, the scaling properties of
 424 κ are consistent with the relative dispersion ones. During August and November, κ scales as δ^2 in the range
 425 below R_d . This indicates the dominance of non-local dispersion at these scales. The transition from the non-
 426 local to the local regime ($\kappa \sim \delta^{4/3}$) is observed for scales close to R_d (and in fact slightly smaller). The estimated
 427 exponent ranges from 1.2 to 1.5 (Fig. 9), and it is smaller in November. The comparison of diffusivity
 428 demonstrates that the freshwater runoff increases the diffusivity in the whole domain.



429
 430 Figure 8: Relative dispersion as a function of time from the release in August (a) and November (b) in linear-
 431 log scales. In this case, particles were released uniformly in the GoT domain. The horizontal lines correspond
 432 to separation distances equal to the Rossby radius R_d .



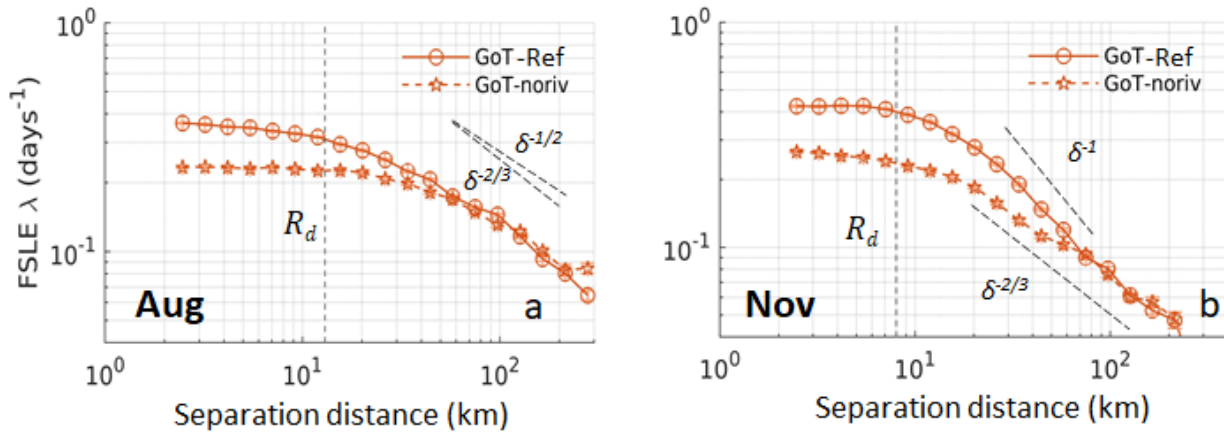
433

434 Figure 9: Relative diffusivity as a function of the separation distance for the two tracking periods in August
 435 (a) and November (b) and for the two model configurations (with and without river discharge). In this case,
 436 particles were released uniformly in the GoT domain. The vertical lines correspond to separation distances
 437 equal to the Rossby radius R_d .

438 The FSLE curves λ as a function of δ shown in Fig. 10 reveal a larger difference in dispersion scaling behaviors
 439 between the two periods of the study. A common feature for both seasons is a transition from a non-local
 440 dispersion regime to a local dispersion one, occurring at a separation distance close to the Rossby radius R_d .
 441 The exponential growth of separation distance below R_d gives an e-folding time of 1.2 – 1.3 days for the GoT-
 442 Ref model and 1.7 – 2.2 days for the GoT-noriv configuration (Fig. 10), in fair agreement with the
 443 corresponding estimate obtained from relative dispersion (Fig. 8).

444 At larger scales (above R_d), a scaling slightly less steep than $\delta^{-2/3}$ and close to $\delta^{-1/2}$ is observed in August,
 445 likely due to relatively small-scale coherent structures that steepen the kinetic energy spectrum to k^{-2} (see,
 446 e.g., Capet et al., 2008). Note that in the GoT-noriv case the corresponding curve is less steep. Therefore, these
 447 results point to the enhancement of the particle spreading at scales comparable or smaller than R_d , in the
 448 simulation including the river discharge. The largest difference between the two configurations is observed at
 449 small scales. It appears that including the river contributions enhances stirring and shortens the dispersion time
 450 by the factor of two in this range of scales (Fig. 10a).

451 The FSLE curves in November show rather different behavior. Above 20 km, the FSLE in both GoT-Ref and
 452 GoT-noriv cases indicates a scale dependent dispersion rate in a broad range of scales. In GoT-Ref case, the
 453 FSLE scales as δ^{-1} (ballistic regime) until $\delta \sim 70$ km, which reveals a strong shear dispersion. This can be
 454 explained by the tendency of particles to be concentrated in the western gulf where the coastal current
 455 contributes to the rapid southward transport. At scales above 70 km, for both the full model and the GoT-noriv
 456 one, the FSLE is perhaps closer to $\delta^{-2/3}$. In the larger scale ranges, the dispersion rate in November is on average
 457 slightly lower than in August (Fig. 10b).

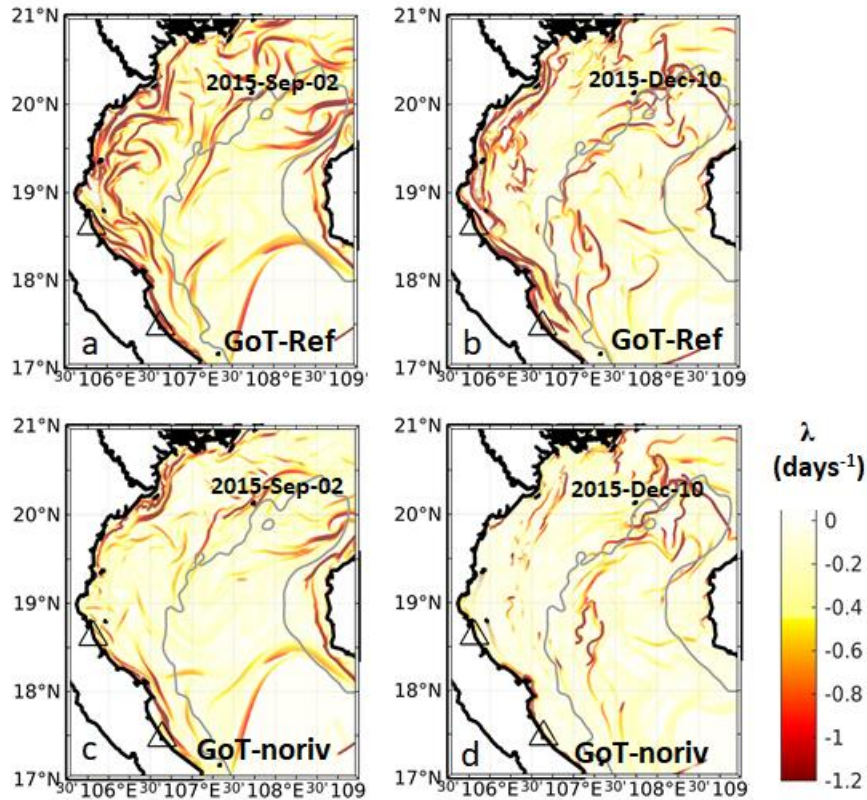


458
 459 Figure 10: FSLE $\lambda(\delta)$ versus the separation distance δ in August (a) and November 2015 (b), for particles
 460 released uniformly in the GoT domain. The vertical lines correspond to separation distances equal to the
 461 Rossby radius R_d .

462 4.3. Lagrangian Coherent structures in the GoT

463 Among different Lagrangian diagnostics, FSLE spatial distributions have been widely used in the analysis of
 464 ocean transport and mixing since they can reveal the hidden transport structures of the flow field. The
 465 characteristic lines with large FSLE values can show the location of Lagrangian coherent structures (LCS)
 466 organizing the transport processes in the GoT. They are sought as the barriers along which the advected
 467 particles are concentrated. Here, we analyze FSLE maps after 30 days of backward integration using the model
 468 simulation. In Fig. 11, the FSLE distribution is shown for two particular dates, September 02 and December
 469 10. The figure demonstrates a complexity of the transport and turbulent dispersion. The FSLE fields are
 470 organized in thin filament-like features with high values (0.6 – 1.2 days⁻¹). The LCSs shaped by these lines
 471 reveal a frontal zone of 25 km wide along the Vietnamese shore in both periods. Long and highly tangled ridge
 472 lines evidence the variability of the flow field there (Fig. 11a). Another region showing a large number of
 473 FSLE ridge lines is located further (~100 km) offshore. Most of the ridge lines in this region seem to be aligned
 474 along 50 m isobath (Fig. 11b).

475 In contrast to the full model, the LCSs derived from the GoT-noriv model simulation clearly lack many small-
 476 scale features in the coastal region. In addition, they indicate much weaker transport barriers (convergence
 477 zones) in the offshore region. FSLE ridge lines appear sparse and characterized by lower values compared to
 478 the full model simulation at the same period (Fig. 11c, d).



479

480 Figure 11: FSLE distribution for two particular dates on September 02 and December 10 using two model
 481 simulations. Gray line shows 50 m isobath.

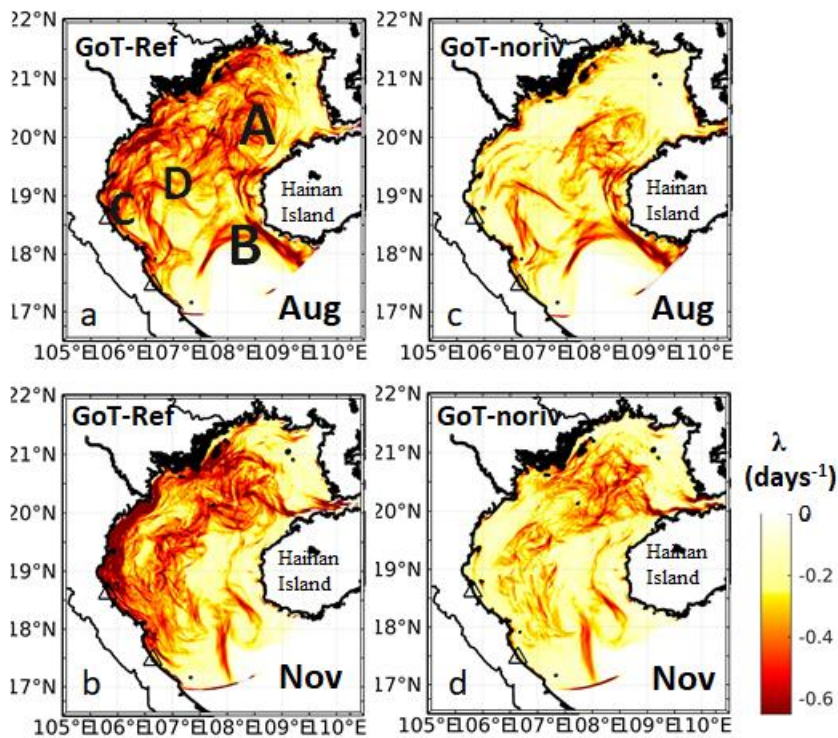
482 Each map of FSLE provides information on short-lived processes. The temporal average of the FSLE maps
 483 over different periods contains a signature of the low-frequency and longer-lived processes. In addition, such
 484 FSLEs provide information on the dispersion time scale. In other terms, the areas with high FSLE values are
 485 characterized by more intense horizontal stirring (Carrasco et al., 2012). We assessed the spatial variability of
 486 dispersion in the GoT by time averaging thirty FSLE maps for two periods. Several regions of high density of
 487 ridge lines can be seen in both seasons with the values of λ ranging from (0.2 to 0.6 days⁻¹). Here we focus on
 488 four geographical regions: the northern gulf (A), the southern gulf (B), nearshore (C) and middle gulf region
 489 (D). It can be seen that regions of intense dispersion ($\lambda = 0.6$ days⁻¹) are found in the northern gulf (location
 490 A) and along the shore (location B) characterized by also by the largest number of filaments and eddies (Fig.
 491 12).

492 In August, thin ridge lines also indicate an intense dispersion in the north and middle regions (location A and
 493 C). Another interesting feature is a quasi-permanent ridge line with $\lambda = 0.6$ days⁻¹ (location B) matching the
 494 location of a loop in the flow incoming from the southern boundary (Fig. 2b).

495 In November, the FSLE maps reveal two regions of intense dispersion located along the middle of the Vietnam
 496 coast (region C) and further offshore (region D) with λ ranging from 0.5 to 0.6 days⁻¹. The ridge lines in these
 497 two regions indicate the effect of the coastal jet and the branch of the current, originating from Hainan strait
 498 (Fig. 2e), on horizontal dispersion. Moreover, spreading of the ridge lines in location D (Fig. 12b) reveals large
 499 spatial variability of dispersion rate within an offshore band of 25-50 km large. LCSs can persist for up to

500 several days thus limiting the exchange between the coastal and offshore regions located west and east of the
501 ridge lines concentrated in sector D (Fig. 12b).

502 The intensity of stirring, which can be identified by taking the spatial average of the FSLEs over the whole
503 area (d'Ovidio et al., 2004), is approximately 0.4 days^{-1} in the GoT-ref model. In the absence of the river
504 discharge, the intensity of stirring decreases by roughly two times on average, down to 0.2 days^{-1} . These
505 average values are reasonably in agreement with the FSLE plateau values λ_L at small scales from Fig. 10.



506

507 Figure 12: 30-day mean FSLEs for the period of August and November from the two model simulations:

508 GoT-Ref (a, b) and GoT-noriv (c, d)

509 5. Discussion

510 In this study, we focus on the analysis of turbulent dispersion regimes and on the identification of LCSs in the
511 GoT from realistic simulations using an approach based on particle pair dispersion. The analysis of relative
512 dispersion is of great importance for the assessment of turbulent stirring in the open and coastal ocean at
513 different spatial and temporal scales. Thus, the main objective of this study was to quantify the turbulent
514 dispersion in the GoT, which is characterized by complex and multiscale dynamics, modulated by the monsoon
515 wind and large buoyant input from a number of rivers (the largest being from the Red River). To the best of
516 our knowledge, this problem has not been addressed yet in this region. Recent advances in the realism of the
517 coastal modeling and observations using coastal radars allow the investigation of the turbulent dispersion using
518 synthetic drifters advected in the radar and model velocity fields. Analysis of turbulent dispersion is performed
519 for two periods, August and November 2015, representing typical summer and winter weather and river
520 discharge conditions. Compared to other velocity data such as geostrophic currents from AVISO products,

521 HFR measurements provide a near-real time, higher space-time resolution (6 km resolution, hourly data
522 compared to roughly 27 km spatial resolution, daily data from AVISO). These data are more suitable for the
523 quantification of the dispersion processes in the GoT. Our result indicates that relative dispersion statistics
524 derived from the HFR tracking of particles are comparable to those obtained from the model. However, the
525 spatial resolution of the HFR-derived velocity fields is still low compared to that of the model. As the short
526 time and small-scale dispersion are sensitive to the details of the flow field, the coarse resolution of the HFR
527 data makes the exploration of small-scale features difficult. In the small-scale ranges, the dispersion rate
528 estimated from the radar measurements is significantly lower than the one from the model simulations in
529 November (e-folding time of approximately 2 and 1 days, respectively).

530 Analysis of relative dispersion, relative diffusivity and FSLE from the numerical model indicated an
531 exponential regime at sub-mesoscale which is consistent with estimations of these quantities for other ocean
532 basins (Beron- Vera & LaCasce, 2016; Berti et al., 2011; Essink et al., 2019; van Sebille et al., 2015). At this
533 scale, the e-folding time estimated using the relative dispersion and the FSLE is similar for both seasons but
534 appears strongly dependent on the river runoff (e-folding time of roughly 1.25 days for the full model and 2.5
535 days in the GoT-noriv model simulation). At larger scales, the dispersion exhibits a scale-dependent behavior
536 indicative of either Richardson local dispersion or ballistic separation, controlled by strong mean currents.
537 Such a transition between regimes occurs at scales close to the Rossby radius of deformation. In general, the
538 pair dispersion properties in the GoT, obtained from the analysis of three Lagrangian diagnostics (relative
539 dispersion, relative diffusivity and FSLE), are consistent with the results of previous studies, based on the
540 analysis of the global drifter dataset (Corrado et al., 2017).

541 It is argued that a super diffusive regime can occur in the presence of strong shear and is characterized by the
542 power law behavior $\sim t^\gamma$ ($\gamma > 1$), as reported in some other studies performed in different regions: in the
543 Adriatic Sea, γ is found ~ 1.8 (Haza et al., 2008), in the Gulf of California, $\gamma \sim 1.9$ (Zavala Sansón, 2015). In
544 our case, γ is found larger, ~ 2.2 . However, rather clear hints to Richardson regime ($\gamma = 3$) are also found over
545 some scale subranges for both model configurations, with and without river discharge.

546 In regions characterized by strong sub-mesoscale dynamics, different limiting FSLE values were found for
547 scales $\delta < 10$ km: $\lambda_L \sim 1 - 1.1$ days⁻¹ in the Gulf of Mexico, (Choi et al., 2017), or $\lambda_L \sim 0.6$ days⁻¹ in the Liguro
548 basin (Schroeder et al., 2011). In the Gulf of La Spezia, the value of λ_L can readily reach 2.5 days⁻¹ (Haza et
549 al., 2012). In our case, the value of λ_L for the same scales ($\delta < 10$ km) is clearly weaker, ranging from 0.3 to
550 0.4 days⁻¹. This indicates that the contribution of sub-mesoscale motions in turbulent dispersion in the Gulf of
551 Tonkin is weak. This seems reasonable because the GoT is a quite shallow basin with limited potential energy
552 which can be stored in the mixed layer where small eddies can be hashed by the wind. Our results are in
553 agreement with those previous studies which reported and demonstrated that dispersion at the sub-mesoscale
554 can be induced non-locally by mesoscale motions (e.g., Haza et al., 2008, Poje et al., 2010). However, it should
555 be noted that the model resolution in the GoT (1 – 2 km in the offshore area to 4.5 km at the open ocean
556 boundary) probably prohibits the exploration of the local stirring generated by small-scale turbulent motions.

557 The impact of the river discharge on the surface dynamics of the GoT is explored using the model simulation
558 with and without rivers runoff. During both periods considered, the river input in the model enhances the
559 dispersion in a wide range of scales, from sub-mesoscale up to 50 km. The river discharge causes a significant
560 change of e-folding time, which decreases from roughly 2.5 days to 1.25 days. The river discharge (when
561 introduced in the model) creates buoyancy gradients and enhances the sub-mesoscale dynamics which in turn
562 modifies the Lagrangian statistics. However, the difference between two numerical experiments, with and
563 without river discharge, was not found to significantly alter the dispersion scaling behaviors. A possible reason
564 could be that we examined statistics averaged over all particle pairs in the whole domain, while the river
565 discharge only enhances the dispersion close to the western coast and locally affects the particles released
566 there.

567 Lastly, we quantified the horizontal stirring caused by small-scale motions using the spatial distribution of
568 FSLEs in different seasons. The LCSs, identified from backward FSLEs using the model velocity field, were
569 analyzed to assess the horizontal stirring by small-scale processes, and appear to be very sensitive to the river
570 forcing. Moreover, the FSLE maps clearly show the regionality of small-scale motions and their impact on
571 dispersion processes. In August, a large concentration of FSLE ridge lines is found in the northern gulf and in
572 the southern gulf where the transport and dispersion are strongly influenced by the incoming flow from the
573 southern open boundary. During August, when the river discharge is at its peak, the river plume is driven
574 northward and can detach from the coast due to the persistent southwest wind (Nguyen-Duy et al., 2021). The
575 surface layer is then decoupled from the subsurface layer. This creates favorable conditions for the
576 development of sub-mesoscale motions via roll-up instabilities of larger scale structures (Klein et al., 2011;
577 Rouillet et al., 2012; Berti et al., 2021). Alternatively, sub-mesoscale motions could be also generated by a
578 complex topography in the northern gulf (small islands, complex bathymetry, etc.). This can explain a high
579 concentration of large FSLE values in the vicinity of the Red river in the GoT-Ref model (location A in Fig.
580 11a). In winter, the spatial distribution of FSLEs reveals the existence of another region of high concentration
581 of FSLE ridge lines matching the outer limit of the coastal current which strongly affects the dispersion
582 processes by organizing the particle distribution.

583 **6. Summary**

584 Relative dispersion in the coastal ocean environment, characterized by a wide range of scales of flow variability
585 is still largely unknown. At scales less than a few km, the dispersion processes have been experimentally
586 investigated using surface drifters in a number of limited size coastal regions. The experimental assessment of
587 turbulent dispersion at larger scales is difficult to realize due to the cost of such experiments. In the present
588 study, we adopted an alternative approach and investigated the turbulent dispersion and transport pathways in
589 the GoT by using a large number of virtual drifters advected in the velocity fields derived from a high-
590 resolution numerical model and HFR measurements.

591 For both types of fields, the results revealed a high degree of consistency regarding the dispersion regime at
592 scales larger than 20 km. At smaller scales, the dispersion rate in the radar velocity field appeared two times
593 lower which is explained by the comparatively low spatial resolution of radar measurements.

594 The Rossby radius of deformation, R_d , is a key lengthscale that separates the regimes of turbulent dispersion.
595 It was estimated from numerical simulations in the GoT performed by Nguyen-Duy et al. (2021). Our results
596 revealed a non-local dispersion regime at scales below R_d and local dispersion at larger scales, which is in
597 agreement with the results of earlier investigations performed in different world oceans (e.g., Haza et al., 2008;
598 Corrado et al., 2017).

599 The seasonal variability in transport patterns and dispersion regimes was further characterized. The time
600 evolution of dispersion showed an exponential growth during first 5 – 8 days of drift for both seasons, followed
601 by a power law regime during the next 6 to 20 days. The ballistic regime was found to dominate the dispersion
602 at mesoscales in winter while Richardson super diffusion regime was diagnosed in summer. This change in
603 regime is mainly related to a combined effect of river discharge and summer monsoon wind which enlarges
604 the river plume area and enhances stirring in the coastal region extending up to 100 km offshore. In November,
605 the ballistic regime is probably induced by strong northeastern monsoon wind providing the coastal current
606 strengthening and local shear dispersion intensification. The non-local dispersion regime (in sub-mesoscale
607 range) was not clearly identified, suggesting that the mesoscale circulation in the GoT largely governs the
608 dispersion at small scales.

609 Four regions with high level of dispersion were identified in the GoT: a nearshore region under the fresh-water
610 influence, an offshore region distant by ~100 km from the coast, a central part of the northern gulf, and a region
611 close to the southern gulf entrance. A seasonality in dispersion strength, caused by the variability of wind
612 forcing and freshwater input by the Red river, was detected.

613 Summarizing, the Lagrangian diagnostics appeared very useful for characterization of turbulent dispersion
614 regimes and identification of regions of high stirring. This is of primary importance for applications involving
615 multi-scale interactions in the coastal ocean, the transport of particulate biological or anthropogenic material.

616 **Acknowledgments**

617 This study was supported by the University of Littoral Côte d'Opale and the Région "Hauts-de-France" PhD
618 fellowship. Chl-a data were provided by ACRI, GlobColour products (<https://hermes.acri.fr/>). We would like
619 to thank Tran Trung Kien for help with the data.

620 **Authors' contributions**

621 M.C.T, A.S, S.B contributed to the conception and scientific design of the study. M.C.T performed the data
622 analysis and wrote the original version of the manuscript. A.S, S.B and N.A deeply involved in the analysis,

623 manuscript organization, and co-writing. N.A and T.ND developed and provided the numerical model results.
624 All authors actively contributed, comments and revised the manuscript.

625 **Funding**

626 This study was funded by Université du Littoral-Côte d'Opale for PhD scholarship fellowship.

627 **Conflict of interest**

628 The authors declare that they have no conflict of interest.

629 **References**

- 630 Artale, V., Boffetta, G., Celani, A., Cencini, M., & Vulpiani, A. (1997). Dispersion of passive tracers in
631 closed basins: Beyond the diffusion coefficient. *Physics of Fluids*, 9(11), 3162–3171.
632 <https://doi.org/10.1063/1.869433>
- 633 Beron-Vera, F. J., & LaCasce, J. H. (2016). Statistics of simulated and observed pair separations in the Gulf
634 of Mexico. *Journal of Physical Oceanography*, 46(7), 2183–2199. <https://doi.org/10.1175/JPO-D-15-0127.1>
- 636 Berta, M., Ursella, L., Nencioli, F., Doglioli, A. M., Petrenko, A. A., & Cosoli, S. (2014). Surface transport
637 in the Northeastern Adriatic Sea from FSLE analysis of HF radar measurements. *Continental Shelf*
638 *Research*, 77, 14–23. <https://doi.org/10.1016/j.csr.2014.01.016>
- 639 Berta, M., Griffa, A., Haza, A. C., Horstmann, J., Huntley, H. S., Ibrahim, R., Lund, B., Özgökmen, T. M., &
640 Poje, A. C. (2020). Submesoscale Kinematic Properties in Summer and Winter Surface Flows in the
641 Northern Gulf of Mexico. *Journal of Geophysical Research: Oceans*, 125(10).
642 <https://doi.org/10.1029/2020JC016085>
- 643 Berti, S., Santos, F. A. Dos, Lacorata, G., & Vulpiani, A. (2011). Lagrangian Drifter Dispersion in the
644 Southwestern Atlantic Ocean. *Journal of Physical Oceanography*, 41(9), 1659–1672.
645 <https://doi.org/10.1175/2011JPO4541.1>
- 646 Berti, S., & Lapeyre, G. (2021). Lagrangian pair dispersion in upper-ocean turbulence in the presence of
647 mixed-layer instabilities. *Physics of Fluids*, 33(3), 036603. <https://doi.org/10.1063/5.0041036>
- 648 Capet, X., McWilliams, J.C., Molemaker, M.J. & Shchepetkin, A.F. (2008). Mesoscale to submesoscale
649 transition in the California current system. Part I: flow structure, eddy flux, and observational tests. *J.*
650 *Phys. Oceanogr.* 38, 29–43. <https://doi.org/10.1175/2007JPO3671.1>
- 651 Corrado, R., Lacorata, G., Palatella, L., Santoleri, R., & Zambianchi, E. (2017). General characteristics of
652 relative dispersion in the ocean. *Scientific Reports*, 7(1), 46291. <https://doi.org/10.1038/srep46291>
- 653 Choi, J., Bracco, A., Barkan, R., Shchepetkin, A. F., McWilliams, J. C., & Molemaker, J. M. (2017).
654 Submesoscale dynamics in the Northern Gulf of Mexico. Part III: Lagrangian implications. *Journal of*
655 *Physical Oceanography*, 47(9), 2361–2376. <https://doi.org/10.1175/JPO-D-17-0036.1>
- 656 D'Asaro, E. A., Shcherbina, A. Y., Klymak, J. M., Molemaker, J., Novelli, G., Guigand, C. M., Haza, A. C.,
657 Haus, B. K., Ryan, E. H., Jacobs, G. A., Huntley, H. S., Laxague, N. J. M., Chen, S., Judt, F.,
658 McWilliams, J. C., Barkan, R., Kirwan, A. D., Poje, A. C., & Özgökmen, T. M. (2018). Ocean
659 convergence and the dispersion of flotsam. *Proceedings of the National Academy of Sciences*, 115(6),
660 1162–1167. <https://doi.org/10.1073/PNAS.1718453115>

- 661 Haza, A. C., Poje, A. C., Özgökmen, T. M., & Martin, P. (2008). Relative dispersion from a high-resolution
662 coastal model of the Adriatic Sea. *Ocean Modelling*, 22(1–2), 48–65.
663 <https://doi.org/10.1016/j.ocemod.2008.01.006>
- 664 d’Ovidio, F., Della Penna, A., Trull, T. W., Nencioli, F., Pujol, M.-I., Rio, M.-H., Park, Y.-H., Cotté, C.,
665 Zhou, M., & Blain, S. (2015). The biogeochemical structuring role of horizontal stirring: Lagrangian
666 perspectives on iron delivery downstream of the Kerguelen Plateau. *Biogeosciences*, 12(19), 5567–
667 5581. <https://doi.org/10.5194/bg-12-5567-2015>
- 668 Essink, S., Hormann, V., Centurioni, L. R., & Mahadevan, A. (2019). Can we detect submesoscale motions
669 in drifter pair dispersion? *Journal of Physical Oceanography*, 49(9), 2237–2254.
670 <https://doi.org/10.1175/JPO-D-18-0181.1>
- 671 Foussard, A., Berti, S., Perrot, X., & Lapeyre, G. (2017). Relative dispersion in generalized two-dimensional
672 turbulence. *Journal of Fluid Mechanics*, 821, 358–383. <https://doi.org/10.1017/jfm.2017.253>
- 673 Haller, G., & Yuan, G. (2000). Lagrangian coherent structures and mixing in two-dimensional turbulence.
674 *Physica D: Nonlinear Phenomena*, 147(3–4), 352–370. [https://doi.org/10.1016/S0167-2789\(00\)00142-1](https://doi.org/10.1016/S0167-2789(00)00142-1)
- 675 Haza, A. C., Poje, A. C., Özgökmen, T. M., & Martin, P. (2008). Relative dispersion from a high-resolution
676 coastal model of the Adriatic Sea. *Ocean Modelling*, 22(1–2), 48–65.
677 <https://doi.org/10.1016/j.ocemod.2008.01.006>
- 678 Haza, A. C., Özgökmen, T. M., Griffa, A., Molcard, A., Poulain, P.-M., & Peggion, G. (2010). Transport
679 properties in small-scale coastal flows: relative dispersion from VHF radar measurements in the Gulf of
680 La Spezia. *Ocean Dynamics*, 60(4), 861–882. <https://doi.org/10.1007/s10236-010-0301-7>
- 681 Haza, A. C., Özgökmen, T. M., & Hogan, P. (2016). Impact of submesoscales on surface material
682 distribution in a gulf of Mexico mesoscale eddy. *Ocean Modelling*, 107, 28–47.
683 <https://doi.org/10.1016/j.ocemod.2016.10.002>
- 684 Klein, P., & Lapeyre, G. (2009). The oceanic vertical pump induced by mesoscale and submesoscale
685 turbulence. *Annual Review of Marine Science*, 1(1), 351–375.
686 <https://doi.org/10.1146/annurev.marine.010908.163704>
- 687 Koszalka, I., LaCasce, J. H., & Orvik, K. A. (2009). Relative dispersion in the Nordic Seas. *Journal of*
688 *Marine Research*, 67(4), 411–433. <https://doi.org/10.1357/002224009790741102>
- 689 LaCasce, J. H. (2008). Statistics from Lagrangian observations. *Progress in Oceanography*, 77(1), 1–29.
690 <https://doi.org/10.1016/j.pocean.2008.02.002>
- 691 Lacroix, G., Maes, G. E., Bolle, L. J., & Volckaert, F. A. M. (2013). Modelling dispersal dynamics of the
692 early life stages of a marine flatfish (*Solea solea* L.). *Journal of Sea Research*, 84, Lumpkin, R., &
693 Elipot, S. (2010). Surface drifter pair spreading in the North Atlantic. *Journal of Geophysical Research*,
694 115(C12), C12017. <https://doi.org/10.1029/2010JC006338>
- 695 Lyard, F. H., Allain, D. J., Cancet, M., Carrère, L., & Picot, N. (2021). FES2014 global ocean tide atlas:
696 design and performance. *Ocean Science*, 17(3), 615–649. <https://doi.org/10.5194/os-17-615-2021>
- 697 Marsaleix, P., Auclair, F., & Estournel, C. (2006). Considerations on open boundary conditions for regional
698 and coastal ocean models. *Journal of Atmospheric and Oceanic Technology*, 23(11), 1604–1613.
699 <https://doi.org/10.1175/JTECH1930.1>
- 700 Marsaleix, P., Auclair, F., Floor, J. W., Herrmann, M. J., Estournel, C., Pairaud, I., & Ulses, C. (2008).
701 Energy conservation issues in sigma-coordinate free-surface ocean models. *Ocean Modelling*, 20(1),
702 61–89. <https://doi.org/10.1016/j.ocemod.2007.07.005>
- 703 Meyerjürgens, J., Ricker, M., Schakau, V., Badewien, T. H., & Stanev, E. V. (2020). Relative Dispersion of
704 Surface Drifters in the North Sea: The Effect of Tides on Mesoscale Diffusivity. *Journal of G*
- 705 Nguyen-Duy, T., Ayoub, N. K., Marsaleix, P., Toubanc, F., De Mey-Frémaux, P., Piton, V., Herrmann, M.,
706 Duhaut, T., Tran, M. C., & Ngo-Duc, T. (2021). Variability of the Red River Plume in the Gulf of To
- 707 Piton, V., Ouillon, S., Vinh, V. D., Many, G., Herrmann, M., & Marsaleix, P. (2020). Seasonal and tidal
708 variability of the hydrology and suspended particulate matter in the Van Uc estuary, Red River,
709 Vietnam. *Journal of Marine Systems*, 211, 103403. <https://doi.org/10.1016/j.jmarsys.2020.103403>

- 710 Piton, V., Herrmann, M., Marsaleix, P., Duhaut, T., Ngoc, T. B., Tran, M. C., Shearman, K., & Ouillon, S.
711 (2021). Influence of winds, geostrophy and typhoons on the seasonal variability of the circulation in the
712 Gulf of Tonkin: A high-resolution 3D regional modeling study. *Regional Studies in Marine Science*,
713 45, 101849. <https://doi.org/10.1016/j.rsma.2021.101849>
- 714 Poje, A. C., Haza, A. C., Özgökmen, T. M., Magaldi, M. G., & Garraffo, Z. D. (2010). Resolution dependent
715 relative dispersion statistics in a hierarchy of ocean models. *Ocean Modelling*, 31(1–2), 36–50.
716 <https://doi.org/10.1016/j.ocemod.2009.09.002>
- 717 Poje, A. C., Özgökmen, T. M., Lipphardt, B. L., Haus, B. K., Ryan, E. H., Haza, A. C., Jacobs, G. A.,
718 Reniers, A. J. H. M., Olascoaga, M. J., Novelli, G., Griffa, A., Beron-Vera, F. J., Chen, S. S., Coelho,
719 E., Hogan, P. J., Kirwan, A. D., Huntley, H. S., & Mariano, A. J. (2014). Submesoscale dispersion in
720 the vicinity of the Deepwater Horizon spill. *Proceedings of the National Academy of Sciences of the*
721 *United States of America*, 111(35), 12693–12698. <https://doi.org/10.1073/pnas.1402452111>
- 722 Roulet, G., McWilliams, J. C., Capet, X., & Molemaker, M. J. (2012). Properties of steady geostrophic
723 turbulence with isopycnal outcropping. *Journal of Physical Oceanography*, 42(1), 18–38.
724 <https://doi.org/10.1175/JPO-D-11-09.1>
- 725 Rogowski, P., Zavala-Garay, J., Shearman, K., Terrill, E., Wilkin, J., & Lam, T. H. (2019). Air-Sea-Land
726 Forcing in the Gulf of Tonkin: Assessing Seasonal Variability Using Modern Tools. *Oceanography*,
727 32(2), 150–161. <https://doi.org/10.5670/oceanog.2019.223>
- 728 Sansón, L. Z., Pérez-Brunius, P., & Sheinbaum, J. (2016). Surface relative dispersion in the southwestern
729 Gulf of Mexico. *Journal of Physical Oceanography*, 47(2), 387–403. [https://doi.org/10.1175/JPO-D-16-](https://doi.org/10.1175/JPO-D-16-0105.1)
730 [0105.1](https://doi.org/10.1175/JPO-D-16-0105.1)
- 731 Schroeder, K., Haza, A. C., Griffa, A., Özgökmen, T. M., Poulain, P. M., Gerin, R., Peggion, G., & Rixen,
732 M. (2011). Relative dispersion in the Liguro-Provençal basin: From sub-mesoscale to mesoscale. *Deep*
733 *Sea Research Part I: Oceanographic Research Papers*, 58(3), 209–228.
734 <https://doi.org/10.1016/j.dsr.2010.11.004>
- 735 Schroeder, K., Chiggiato, J., Haza, A. C., Griffa, A., Zgkmen, T. M., Zanasca, P., Molcard, A., Borghini, M.,
736 Poulain, P. M., Gerin, R., Zambianchi, E., Falco, P., & Trees, C. (2012). Targeted Lagrangian sampling
737 of submesoscale dispersion at a coastal frontal zone. *Geophysical Research Letters*, 39(11), 4–9.
738 <https://doi.org/10.1029/2012GL051879>
- 739 Tran, M. C., Sentchev, A., & Nguyen, K. C. (2021). Multi-scale variability of circulation in the Gulf of
740 Tonkin from remote sensing of surface currents by high-frequency radars. *Ocean Dynamics*, 71(2),
741 175–194. <https://doi.org/10.1007/s10236-020-01440-x>
- 742 Yaremchuk, M., & Sentchev, A. (2011). A combined EOF/variational approach for mapping radar-derived
743 sea surface currents. *Continental Shelf Research*, 31(7–8), 758–768.
744 <https://doi.org/10.1016/j.csr.2011.01.009>
- 745 Zimmerman, J. T. F. (1981). Dynamics, diffusion and geomorphological significance of tidal residual eddies.
746 *Nature*, 290(5807), 549–555. <https://doi.org/10.1038/290549a0>
- 747 Zhong, Y., and A. Bracco (2013), Submesoscale impacts on horizontal and vertical transport in the Gulf of
748 Mexico, *J. Geophys. Res. Oceans*, 118, 5651–5668, doi:10.1002/jgrc.20402